

STOCHASTIC SPECKLE DISCRIMINATION WITH TIME-TAGGED PHOTON LISTS: DIGGING BELOW THE SPECKLE NOISE FLOOR

ALEX B. WALTER¹, CLINTON BOCKSTIEGEL¹, TIMOTHY D. BRANDT¹, BENJAMIN A. MAZIN¹

Draft version June 11, 2019

Abstract

We present an algorithm that uses the distribution of photon arrival times to distinguish speckles from incoherent sources, like planets and disks, in high contrast images. Using simulated data, we show that our approach can overcome the noise limit from fluctuating speckle intensity. The algorithm is likely to be most advantageous when a coronagraph limits the coherent diffraction pattern in the image plane but the intensity is still strongly modulated by fast-timescale uncorrected stellar light, for example from atmospheric turbulence. These conditions are common at small inner working angles and will allow probing of exoplanet populations at smaller angular separations. The technique requires a fast science camera that can temporally resolve the speckle fluctuations, and the detection of many photons per speckle decorrelation time. Since the algorithm directly extracts the incoherent light, standard differential imaging post-processing techniques can be performed afterwards to further boost the signal.

Subject headings:

1. INTRODUCTION

Direct imaging is a challenging exoplanet discovery and characterization technique due to the extreme contrast ($<10^{-4}$ for ground based targets) and small angular separations ($\lesssim 1''$) between the planetary companion and its stellar host. Despite this, adaptive optics (AO) and coronagraphy have enabled the discovery of planets up to $\sim 10^6$ times fainter than their host stars (Marois et al. 2008; Lagrange et al. 2010; Kuzuhara et al. 2013; Macintosh et al. 2015; Keppler et al. 2018). Imaging an exoplanet requires subtracting the light of its host star in the form of the point-spread function (PSF). If this background were static and could be subtracted perfectly, exoplanet imaging would be limited only by the photon shot noise of the bright host star. Instead, high-contrast imaging is limited by uncontrolled scattered and diffracted light, which produces a coherent speckle halo in the image plane (Guyon 2005).

Fast atmospheric speckles average down over an observation, while slower, quasistatic speckles must be removed using post-processing techniques. Angular differential imaging (ADI, Marois et al. 2006) exploits the rotation of the Earth, and hence the field-of-view of an altitude-azimuth telescope, to distinguish diffraction speckles from astrophysical sources. Spectral differential imaging (SDI, Racine et al. 1999; Marois et al. 2000; Sparks & Ford 2002) uses the scaling of diffraction speckles with wavelength. Since the initial development of ADI and SDI, a variety of post-processing algorithms have refined their approaches to dig deeper into the stellar PSF (e.g. Lafrenière et al. 2007; Soummer et al. 2012; Marois et al. 2014).

The time variability and chromaticity of quasi-static speckles limit the performance of ADI and SDI (Gerard et al. 2019). Both techniques also suffer at small separations where exoplanets are more likely to hide. The

speckle spectral dispersion used by SDI is proportional to the separation: close to the star, it becomes smaller than the planet's PSF. For ADI, the arclength traced by the companion's sky rotation is proportional to the separation. Furthermore, the precision of the background estimate for PSF subtraction is limited by low counting statistics at small separations (Mawet et al. 2014). Even without these issues, the variability induced by speckle fluctuations can dominate the photon noise and be well above the shot noise expected from the total number of photons.

Stochastic Speckle Discrimination (SSD, Gladysz & Christou 2008) is a post-processing technique designed to reduce the additional noise caused by speckle fluctuations by temporally resolving them. It relies on the difference in photon arrival time statistics between a planet/extended source and the off-axis residual stellar speckles (Canales & Cagigal 1999; Cagigal & Canales 2001; Aime & Soummer 2004; Fitzgerald & Graham 2006; Soummer et al. 2007). With millisecond imaging cameras, SSD-like approaches have been shown to reduce speckle noise from even fast atmospheric speckles and improve the contrast limit for the detection of substellar companions (Gladysz et al. 2010; Frazin 2016; Meeker et al. 2018; Stangalini et al. 2018).

In this paper, we present an improved version of SSD to exploit noise-free photon-counting cameras like MEC, the Microwave Kinetic Inductance Detector (MKID) Exoplanet Camera (Walter et al. 2018; Meeker et al. 2018) on Subaru Telescope's SCEXAO instrument (Lozi et al. 2018). Our approach statistically distinguishes a combination of constant and speckle intensity (both ultimately from the bright star) from incoherent light (from a planet or disk). At small separations, where ADI and SDI are least effective and the scientific questions are most pressing (Mawet et al. 2012), we expect SSD to offer strong improvements in the limiting detection contrast. This paper describes the new photon counting SSD technique and demonstrates its performance on simulated data.

¹ Department of Physics, University of California, Santa Barbara, Santa Barbara, CA 93106, USA

We organize the paper as follows. In Section 2 we detail the simulation of photon lists to emulate the data expected from photon-counting cameras like MEC. Section 3 describes a formal extension of previous SSD analysis techniques with millisecond images using a maximum likelihood algorithm. We simulate the performance for various atmospheric conditions, planet brightnesses, and effective exposure times. Section 4 presents the new photon-counting SSD algorithm that estimates the incoherent light from a companion or disk directly from individual photon arrival timestamps. We demonstrate the algorithm on a simulated telescope image. We discuss the main results in Section 5, and conclude with Section 6.

2. SIMULATING PHOTON ARRIVAL TIMES

2.1. Modeling the Stellar Speckle Intensity

The statistics governing the off-axis intensity distribution of coherent light with a partially developed speckle pattern have been studied at length. Originally derived by Goodman (1975) and verified experimentally by Cagigal & Canales (2001) and Fitzgerald & Graham (2006), the probability of getting an instantaneous intensity I given I_c and I_s is governed by the Modified Rician (MR) distribution, defined as:

$$\rho_{\text{MR}}[I|I_c, I_s] = \frac{1}{I_s} \exp\left[-\frac{I+I_c}{I_s}\right] I_0\left[\frac{2\sqrt{II_c}}{I_s}\right], \quad (1)$$

where $I_0[x]$ denotes the zero-order modified Bessel function of the first kind. The parameter I_c represents the intensity of the “constant” part of the diffraction pattern, i.e. the PSF of a star without the atmosphere, while I_s is the intensity of the seeing halo which manifests as a “speckle” pattern.

Typically the AO system attempts to confine all the speckles into the constant diffraction pattern. A coronagraph can remove or transform this coherent portion out of the image plane. For all of the calculations in this paper we assume that the Strehl ratio, and by extension I_c and I_s , remain constant.

Speckle intensity is correlated temporally. In the limit of Kolmogorov atmospheric turbulence and frozen flow, the speckle decorrelation time can be thought of as the wind crossing time across the telescope pupil (Macintosh et al. 2005). In reality, the turbulence is not Kolmogorovic and the AO loop and telescope vibrations can further complicate the speckle temporal power spectrum density (PSD) (Stangalini et al. 2016). This may result in a faster speckle decorrelation time, or a temporal PSD described by multiple exponential timescales. For the purposes of this paper we characterize the speckle PSD as a simple exponential decay with a characteristic speckle lifetime of $\tau_s = 0.1$ s to roughly match empirical data in the near infrared (Fitzgerald & Graham 2006; Meeker et al. 2018; Goebel et al. 2018). The speckle lifetime can change drastically depending on the atmospheric conditions but our results here can be qualitatively understood in those cases by scaling all parameters in time. A core condition for the SSD technique is for many photons to arrive in a single speckle decorrelation time: if this is satisfied, individual speckle fluctuations can be probed.

2.2. Modeling an Incoherent Source

A Poisson source incoherent with the stellar light and parameterized by intensity I_p can be injected and the relevant photons uniquely identified in simulation. Any incoherent Poisson sources will be represented by this term, including binary companions, planetary companions, extended sources, dark current, and read noise. In the case that $I_s = 0$, the MR distribution reduces to a Poisson distribution with intensity I_c and will be indistinguishable from I_p . In the demonstrations that follow, we identify I_p as an injected planetary companion.

The intensity fluctuations associated with speckles elevate the noise floor above the typical shot noise, i.e., it is harder to measure the planet’s intensity when it is embedded in a boiling speckle field. If the speckle temporal information is marginalized over, then we show in the Appendix that the total variance of temporally correlated intensities obeying MR statistics combined with photon shot noise is

$$\sigma_{I,\text{tot}}^2 \approx \frac{2\tau_s (I_s^2 + 2I_c I_s) + I_c + I_s + I_p}{T_{\text{tot}}}. \quad (2)$$

The variance of the measured intensity is inversely proportional to the total integration time, T_{tot} , as expected. This is the long exposure ($t_{\text{exp}} \gg \tau_s$) photon noise limit faced by all PSF subtraction techniques like ADI and SDI. In the limit that $2\tau_s I_s \ll 1$, this variance reduces to pure shot noise on the number of photons. For high contrast imaging, typical parameters might be $\tau_s = 0.1$ s, $I_s = 50 \text{ s}^{-1}$, and $2\tau_s I_s = 10$, in which case the noise from speckle fluctuations will dominate. In Section 4, we show that this noise can be overcome by temporally resolving individual fluctuations in the speckle background.

2.3. Generating Mock Photon Lists

We have developed code² for quickly generating mock photon lists with an optional injected planet, corresponding to the output of a single MKID-like pixel which is single photon counting with low noise. The photon lists obey the following rules:

1. The underlying intensities are MR distributed, but are correlated in time with $\langle I(t)I(t+\delta t) - \langle I \rangle^2 \rangle \propto \exp[-\delta t/\tau_s]$.
2. I_c , I_s , and I_p are independently specified by the user, such that I_c and I_s govern the MR statistics of the stellar intensity and I_p is the mean count rate of a Poisson source. The total intensity should have an expectation value of $\langle I \rangle = I_c + I_s + I_p$.
3. Due to the intrinsic dead time in an MKID, photons are removed from the list if they arrive within τ_0 of the previous valid photon’s arrival time.

The procedure for generating photon timestamps begins with creating a correlated list of random numbers that follow a Gaussian distribution. The random numbers are transformed to a uniform distribution ranging from 0 to 1, and finally transformed again to a MR distribution. The correlated MR sequence defines the intensity in photon counts for a small ($\ll \tau_s$) time bin

² Part of the MKID Pipeline python package available at <https://github.com/MazinLab/MKIDPipeline>

(we used $200 \mu\text{s}$), and a Poisson draw on that “instantaneous” intensity determines the number of photons that will finally be placed into that bin. The photons are distributed according to a uniform distribution in each bin. For simplicity, we assume neighboring pixels to have uncorrelated photon lists.

Since MKIDs do not have the same dark current or readout noise as conventional semiconductor detectors we do not add any additional noise. However, during high count rates photons can be lost due to a firmware triggering lockout that acts as a non-paralyzable dead time (van Eyken et al. 2015). We use $\tau_0 = 10 \mu\text{s}$ to match the latest firmware implemented on MEC. This dead time formulation could be used with quasi-photon counting EMCCDs to account for photon pile-up.

3. SSD WITH MILLISECOND IMAGES

Past efforts have been successful in extracting I_c and I_s parameters of astrophysical sources from a series of millisecond images (Fitzgerald & Graham 2006; Gladysz et al. 2010; Meeker et al. 2018). In these experiments images were acquired with a fixed exposure time and the intensities at spatial locations under test were extracted into a light curve like that shown in the top panel of Figure 1. The distribution of intensities formed a histogram to which a modified Rician function could be fit. The middle panel of Figure 1 shows this process for three exposure times. Since faint companions can masquerade as static speckles, a large I_c/I_s ratio can be used as a merit function for planet detection in comparison to the rest of the image field (Gladysz et al. 2010; Meeker et al. 2018).

3.1. Maximum Likelihood Model for Discrete Light Curves

In this section we extend previous work to a more formal approach by finding the best-fit values of I_c , I_s , and I_p with a maximum likelihood algorithm operating on the light curve. This allows for a direct detection of the non-stellar intensity, I_p , in the form of a point source like a planet or an extended source like a protoplanetary disk. Furthermore, we can naturally introduce photon noise from a low-intensity photon counting regime. By allowing the MR distribution in Equation (1) to suffer a Poisson-Mandel transformation (Cagigal & Canales 1999; Aime & Soummer 2004), the discrete stellar intensity distribution becomes

$$\begin{aligned} p_\star[n|I_c, I_s] &= \int_0^\infty \frac{I^n}{n!} \exp[-I] \rho_{\text{MR}}[I] dI \\ &= \frac{1}{I_s + 1} \left(1 + \frac{1}{I_s}\right)^{-n} \exp\left[-\frac{I_c}{I_s}\right] \\ &\quad \times L_n\left[\frac{-I_c}{I_s^2 + I_s}\right] \exp\left[\frac{I_c}{I_s^2 + I_s}\right], \end{aligned} \quad (3)$$

where L_n is the n^{th} Laguerre polynomial. The units of intensity for this section are number of photons per exposure time, t_{exp} . If a planet (or some other source that is incoherent with the star) exists in the field, the intensity distribution at that location will be the discrete convolution of p_\star with the planet’s independent probability distribution p_p . To simplify, we assume the incoherent source has a Poisson probability distribution,

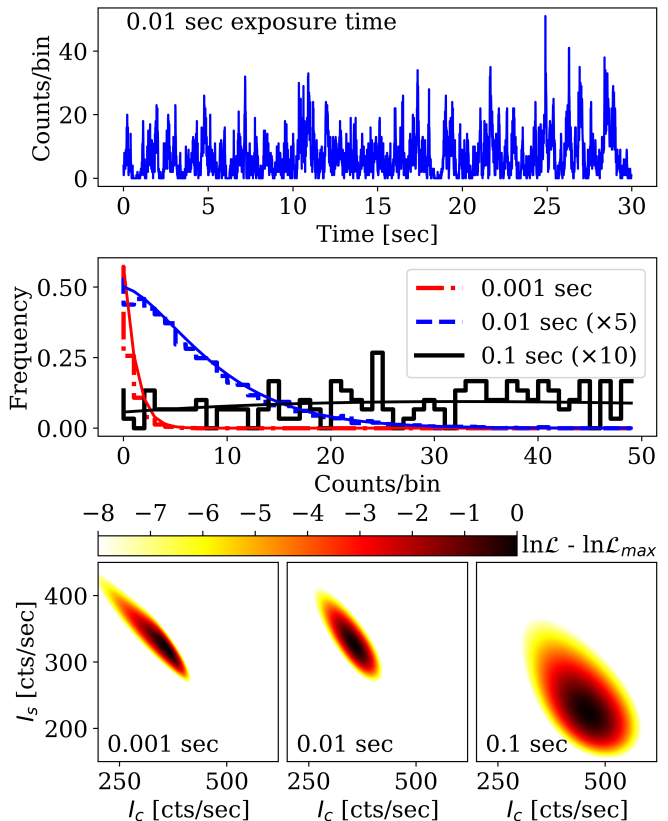


FIG. 1.— Top: a 30 s mock photon list simulated using the parameters $I_c = 300$, $I_s = 300$, $I_p = 0$ photons/s with $\tau_s = 0.1$ s, is binned into 0.01 s exposures to form a light curve. Middle: The same photon list is binned by three different exposure times and used to plot intensity histograms. The best-fit modified Rician functions are overplotted. The distribution changes shape as the bin size is varied; the corresponding fitted parameters also change. The histograms for 0.01 and 0.1 s exposure times have been scaled by factors of 5 and 10 respectively. Bottom: the likelihood is marginalized over I_p for the three different exposure times to illustrate how the best fit parameters evolve with bin size. The darkest area in the plot represents the maximum likelihood and determines the best fit values of I_c and I_s . The same photon list was used for all plots.

$p_p[m|I_p] = \exp[-I_p] I_p^m / m!$ with average intensity I_p . The likelihood of the i th bin of a light curve containing k photons given I_c , I_s , and I_p is

$$\mathcal{L}_i = \sum_{m=0}^{k_i} p_p[m|I_p] p_\star[k_i - m|I_c, I_s], \quad (4)$$

which becomes

$$\begin{aligned} \mathcal{L}_i &= \frac{1}{I_s + 1} \exp\left[-I_p - \frac{I_c I_s}{I_s^2 + I_s}\right] \\ &\quad \times \sum_{m=0}^{k_i} \frac{I_p^m}{m!} \left(1 + \frac{1}{I_s}\right)^{-(k_i - m)} L_{k_i - m}\left[\frac{-I_c}{I_s^2 + I_s}\right]. \end{aligned} \quad (5)$$

The likelihood of the entire light curve is $\mathcal{L} = \prod_i \mathcal{L}_i$. We use a Newton conjugate-gradient search to find the most likely values of I_c , I_s , and I_p .

The maximum likelihood estimate of the intensity distribution is overplotted onto the light curve histograms

for three different exposure times in the middle panel of Figure 1. The bottom panel shows the likelihood functions marginalized over I_p for these three exposure times.

3.2. Performance of Millisecond Imaging SSD

To understand the performance of this millisecond imaging SSD algorithm and the extent to which it can improve exoplanet detections, we produce receiver operator characteristic (ROC) curves (Tanner Jr. & Swets 1954; DeLong et al. 1988; Krzanowski & Hand 2009; Jensen-Clem et al. 2017). We achieve this by generating an ensemble of mock photon lists with the same nominal values of I_c , I_s , and $I_p = 0$ and calculating maximum likelihood estimates to build up a distribution of I_p corresponding to the signal-absent hypothesis. Next we inject a planet with $I_p > 0$ and calculate maximum likelihood estimates to build a distribution for I_p corresponding to the signal-present hypothesis. These distributions are shown in the left column of Figure 2. The cumulative distributions define the false positive and true positive fractions, which in turn define the shape of the ROC curve for a planet with a given intensity.

The right column of Figure 2 demonstrates the performance of the millisecond imaging SSD algorithm for different exposure times. The shape of the discrete intensity distribution can change depending on exposure time, which systematically affects the resulting maximum likelihood estimates (MLE) for I_c , I_s , and I_p along with their uncertainties. In some cases there is a significant probability for the most likely value of I_p to be equal to zero. In the case that $I_c \gg I_s$, the MLE probability can be multimodal with a significant peak at $\text{MLE } I_p \approx \text{True } I_c + \text{True } I_p$. Both these behaviors appear for the same reason: when there is little modulation by I_s of photons associated with I_c , then I_c becomes difficult to distinguish from I_p . However, the total flux is still accurately recovered.

4. SSD IN THE PHOTON COUNTING REGIME

4.1. Maximum Likelihood Model for Photon Arrival Times

We find that there exists an optimal camera frame rate that leads to the most precise probability distribution for I_c , I_s , and I_p . For exposure times that are too long ($t_{\text{exp}} \gg \tau_s$) the speckle temporal information is averaged over. For exposure times that are too short ($t_{\text{exp}} \ll \delta t$, the photon inter-arrival time) the correlation between subsequent photon arrivals is lost because frames are interpreted as an unordered set containing only 0 or 1 photons. In order to avoid this pitfall, we develop the posterior probability for I_c , I_s , and I_p directly from the set of photon inter-arrival times.

We start by considering the (normalized) probability density for the next inter-photon arrival interval, δt , given a fixed intensity I :

$$p[\delta t|I] = Ie^{-I\delta t}. \quad (6)$$

The speckle field intensity is not fixed but varies in time with the modified Rician probability density described in Equation (1). At a fixed point in time, the probability density of the next photon arrival time given I_c and I_s

becomes

$$p[\delta t|I_c, I_s] = \int_0^\infty p[\delta t|I]\rho_{\text{MR}}[I|I_c, I_s]dI, \quad (7)$$

where we have integrated the Poisson probability density from Equation (6) over all possible instantaneous stellar intensities, I . Intensities are considered to be in units of photons per second. We assume here that the speckle lifetime is much longer than the time it takes a photon to arrive, $\tau_s \gg \delta t$.

With a set of photon inter-arrival times, $\{\delta t_i\}$, we want the relative probability that a δt is realized. At moments that happen to have higher instantaneous intensities the number of short δt_i 's will be increased. Thus, the relative probability of a photon inter-arrival time being in our data becomes

$$p[\delta t|I_c, I_s] \propto \int_0^\infty p[\delta t|I]\rho_{\text{MR}}[I|I_c, I_s]IdI. \quad (8)$$

Finally, we consider the case that light incoherent with the star, such as from a planet, is in the field. We consider only the simplest case in which this source has constant intensity I_p and is governed by Poisson statistics. In this case, the relative probability of δt given I_c , I_s , I_p is

$$p[\delta t|I_c, I_s, I_p] \propto \int_0^\infty p[\delta t|I + I_p]\rho_{\text{MR}}[I|I_c, I_s](I + I_p)dI, \quad (9)$$

which can be evaluated analytically. We then find the normalization constant by setting

$$\int_{\tau_0}^\infty p[\tau|I_c, I_s, I_p]d\tau = 1. \quad (10)$$

Equation (10) accounts for the non-paralyzable detector dead time, τ_0 , intrinsic to MKIDs by replacing the lower limit of integration with τ_0 . In Equation (9), we set the likelihood equal to zero for $\delta t < \tau_0$. It is convenient to use the change of variables,

$$u_i = \frac{1}{1 + I_s\delta t_i}, \quad u_{\text{max}} = \frac{1}{1 + I_s\tau_0}. \quad (11)$$

The log-likelihood, $\log(\mathcal{L})[I_c, I_s, I_p]$, then becomes

$$\begin{aligned} \log(\mathcal{L}) &= \sum_{i=1}^N p[\delta t_i|I_c, I_s, I_p] \\ &= \sum_{i=1}^N (u_i - 1) \left(\frac{I_p}{I_s u_i} + \frac{I_c}{I_s} \right) \\ &\quad + \sum_{i=1}^N \log \left[I_c^2 u_i^5 + 4I_c I_s u_i^4 + (2I_s^2 + 2I_p I_c) u_i^3 \right. \\ &\quad \quad \left. + 2I_p I_s u_i^2 + I_p^2 u_i \right] \\ &\quad - N \frac{(u_{\text{max}} - 1)(I_p + I_c u_{\text{max}})}{I_s u_{\text{max}}} \\ &\quad - N \log [I_c u_{\text{max}}^3 + I_s u_{\text{max}}^2 + I_p u_{\text{max}}]. \quad (12) \end{aligned}$$

As in Section 3, we assume that AO performance remains stable so that I_c and I_s remain constant over the course of observations.

Equation (12) for the photon counting SSD algorithm

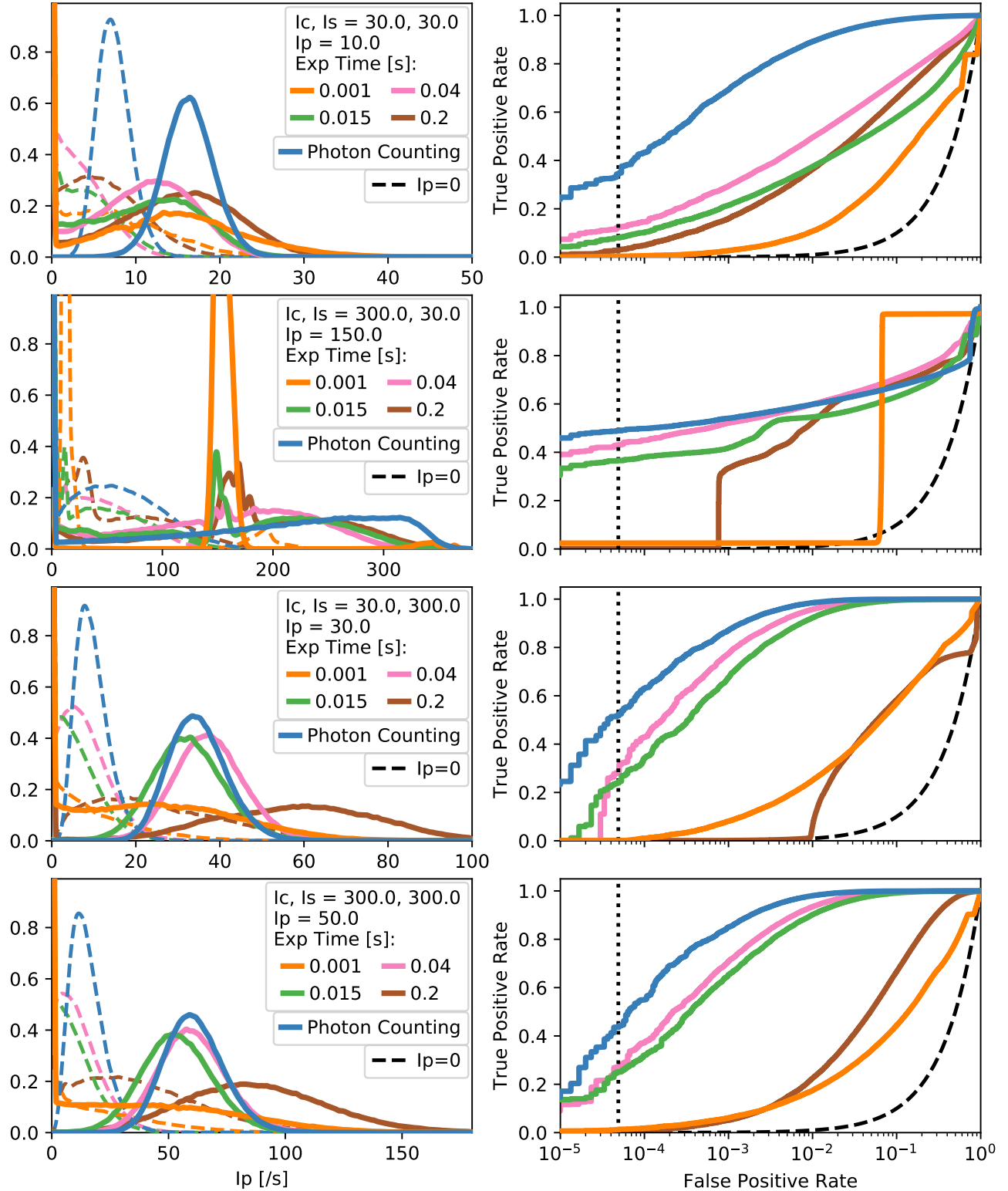


FIG. 2.— Performance of our millisecond imaging SSD algorithm (Section 3) compared to our photon counting SSD algorithm (Section 4). Left panels: histograms of the maximum likelihood estimates of I_p , computed using $3 \cdot 10^5$ 30 s mock photon lists. Maximum likelihood estimates for I_p are calculated for various effective exposure times and for the case with (solid line) and without ($I_p = 0$, dashed line) an injected planet. The y -axis in the left column is arbitrary. The probability distributions are used to calculate the true/false positive rates for the receiver operator characteristic (ROC) curve (right). The vertical dotted line at $1/20000$ (for the 20000 pixels in MEC) roughly indicates the maximum tolerable false positive rate. The full photon-counting SSD algorithm (blue lines) described in Section 4 outperforms the cases with nonzero exposure times.

replaces Equation (5) from Section 3. We use a Newton conjugate-gradient search to find the maximum of the log-likelihood space and recover the best estimates for I_c , I_s , and I_p .

The photon-counting SSD algorithm consistently outperforms the millisecond imaging SSD algorithm from Section 3, which marginalizes over temporal information via the exposure time (see Figure 2). In Figure 3 we show the performance of the photon counting SSD algorithm under conditions given by various combinations of I_c and I_s , and with various planet brightnesses I_p . The algorithm performs well with a high true positive detection rate even for the case when I_c and I_s are both large. However, the performance suffers in the case of $I_c \gg I_s$. As in millisecond imaging SSD, I_p and I_c become indistinguishable in this limit.

4.2. Maximum A Posteriori Estimation

Prior knowledge of a parameter can improve the estimates of I_c , I_s , and I_p . In our case, we commonly have information on the I_c parameter which corresponds to the static or quasi-static speckle point spread function either from a telescope model or measured on a reference star. For such situations, the log likelihood function in Equation (12) can be modified with a Gaussian prior as

$$\log(\mathcal{L}) \rightarrow \log(\mathcal{L}) - \frac{1}{2} \left((I_c - \tilde{I}_c) / \sigma[\tilde{I}_c] \right)^2 \quad (13)$$

where $\tilde{I}_c \pm \sigma[\tilde{I}_c]$ is the prior on I_c . The new estimates of I_c , I_s , and I_p become maximum a posteriori (MAP) estimates.

4.3. Performance on Simulated Telescope Image

We evaluate the performance of the photon-counting SSD algorithm on a simulated 30 s telescope image without a coronagraph. We identify I_c as the Airy-ring pattern of a diffraction limited telescope with a circular unobstructed aperture, I_s as the seeing halo from atmospheric speckles with a Strehl ratio $\Sigma I_c / \Sigma(I_c + I_s) = 0.7$, and I_p as a series of injected planets at various brightnesses and separations. The faintest planet's total intensity is 40 photons/s, for a contrast of $5 \cdot 10^{-5}$ with the host star, and is separated by $3.5 \lambda/D$. Assuming a 5% end-to-end throughput on an 8.2 m telescope, the stellar magnitude in the near infrared is approximately $J = 10$. We assume a speckle decorrelation time of $\tau_s = 0.1$ s and detector dead time of $\tau_0 = 10 \mu\text{s}$.

Each pixel has an independent 30 s photon list generated from the ‘‘True’’ I_c , I_s , and I_p shown in panels (c), (f), and (i) respectively of Figure 4. Spatial correlations in the photon lists are ignored for simplicity. The average intensity realized for each pixel is shown in Figure 4a. Figure 4b is the average intensity minus the expected light from the star, (True $I_c + \text{True } I_s$), which illustrates the best possible long exposure PSF subtraction (compare the background variance to Equation (2)). The MLE I_c , I_s , and I_p are shown in Figure 4d, g, and j respectively. In Figure 4e, h, and k, we calculate the MAP estimates. We used the True $I_c \pm 3 \cdot \sqrt{\text{True } I_c}$ as a Gaussian prior on I_c ; in practice one could use a telescope model or a reference PSF. The central black dot with radius $1.22 \lambda/D$ is not a coronagraph but simply obscures the on-axis light for convenience.

Comparing Figure 4d to Figure 4b shows that the MLE I_p from the photon counting SSD algorithm recovers the injected planets better than a perfect stellar PSF subtraction (i.e. subtraction of the true I_c and I_s). Figure 4d and e show that the MAP estimate for I_p is not significantly better than the MLE I_p (although the MAP estimate for I_c is more precise). This is surprising because the MAP estimate includes a prior on I_c that should help discriminate between I_c and I_p . That this is not the case indicates we can take full advantage of the photon counting SSD algorithm without prior knowledge of the telescope PSF.

For the central pixel of each planet, we used 10^5 independent photon lists to calculate the signal-to-noise ratio $S/N = (\langle I_p \rangle - \langle \text{Background} \rangle) / (\text{std. dev.} \langle I_p \rangle)$ where the $\langle \text{Background} \rangle$ is estimated by not injecting a planet. These are recorded in Table 1. The long exposure photon noise limit is also recorded in Table 1 where the estimated I_p is equal to the total flux minus the light from the star, (True $I_c + \text{True } I_s$). While the results are from the simulated ensemble, they match the results from Equation (2). Table 1 is representative of 30 seconds of data, but the S/N will scale with $\sqrt{T_{\text{tot}}}$. For a 2 minute exposure, all values in Table 1 should be scaled up by a factor of 2. The S/N was calculated using only the central pixel for convenience but would be larger if the surrounding pixels were considered.

5. DISCUSSION

While it remains impossible to beat the photon shot noise \sqrt{N} , Figure 4 shows that the photon counting SSD algorithm can beat the long exposure ($t_{\text{exp}} \gg \tau_s$) photon noise limit described by Equation (2). Table 1 quantifies the improvement in the S/N as a factor of 3 in the case of faintest planet ($5 \cdot 10^{-5}$) at the nearest separation ($3.5 \lambda/D$). This is possible because the speckle fluctuations are temporally resolved ($t_{\text{exp}} \ll \tau_s$) and individual speckles are probed by multiple photons ($\delta t \ll \tau_s$). In the case that the fluctuations from stellar speckles dominate the variance of the total intensity ($2I_s\tau_s \gg 1$), fast, noiseless detectors like MKIDs or EMCCDs are needed to dig beneath the noise. This often occurs in high contrast imaging at small separations (\lesssim seeing radius) and is especially important at $\lesssim 5 \lambda/D$ where ADI and SDI start to lose their effectiveness (depending on spectral coverage, sky rotation, and AO performance).

SSD will benefit ADI and SDI by reducing speckle noise from the data that is fed into those algorithms. ADI processing can be approached the same way as usual, but instead of using raw images one would use the I_p images produced with SSD. The modulation of the planet location will be unaffected by SSD. Similarly for SDI, the algorithm would be given I_p maps at various wavelengths. This approach would require wavelength information for each detected photon, which is an intrinsic feature of an MKID detector.

Our SSD algorithm does not perform well when $I_c \gg I_s$ as seen in Figure 3. In this regime there is little modulation of the static speckle intensity I_c by the atmospheric speckle field I_s , and as a result I_c starts to become indistinguishable from the Poisson distributed I_p . This can be greatly mitigated with a coronagraph and possibly active speckle nulling (Martinache et al. 2014) which

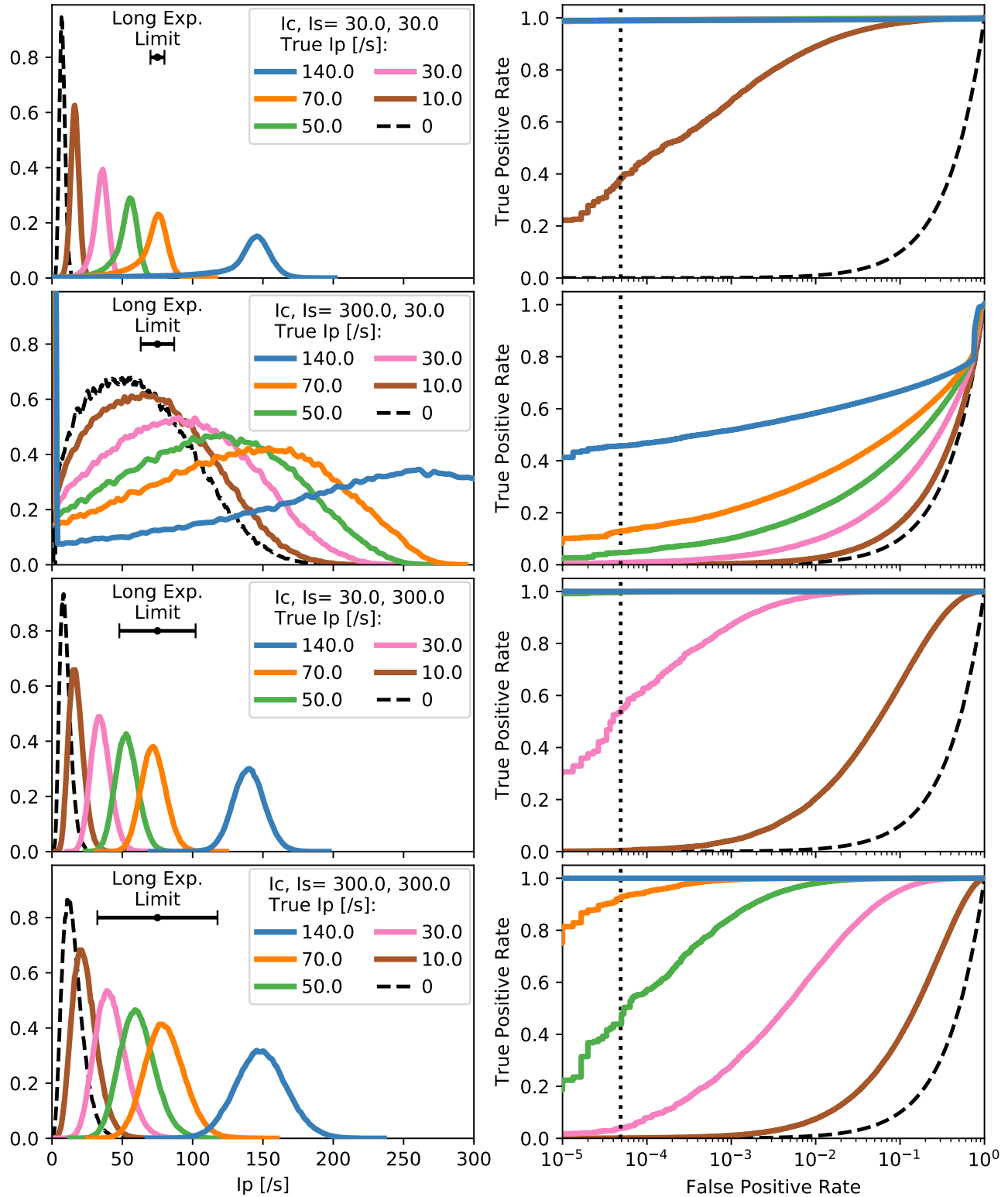


FIG. 3.— Performance of our photon-counting SSD algorithm. Left panels: histograms of the maximum likelihood estimates of I_p , computed using $3 \cdot 10^5$ 30 s mock photon lists for each set of parameters. The $\pm\sigma$ for the long exposure photon noise limit (Equation (2)) is shown with an error bar. The y -axis in the left column is arbitrary. The probability distributions are used to calculate the true/false positive rates for the receiver operator characteristic (ROC) curve (right panels). The vertical dotted line at $1/20000$ (for the 20000 pixels in MEC) roughly indicates the maximum tolerable false positive rate. The algorithm performs well with a high true positive detection rate even for the case when I_c, I_s are both large. However, the performance suffers in the case of $I_c \gg I_s$ (row 2).

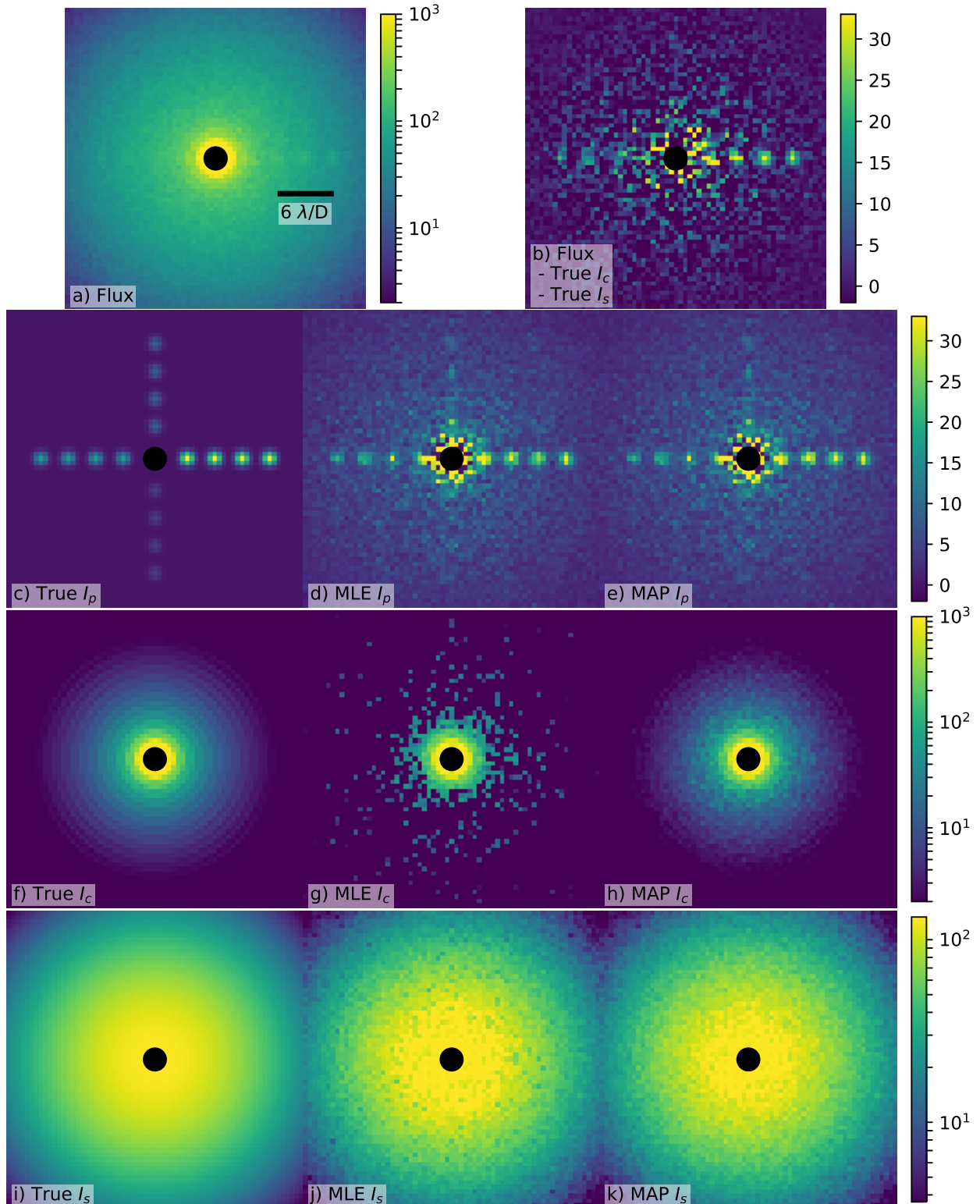


FIG. 4.— Performance of our photon-counting SSD algorithm on simulated telescope images. Panel (a) shows the average intensity of simulated photon lists in each pixel; panels (c), (f), and (i) show the parameters used. Panel (b) subtracts stellar flux from (f) and (i) from the average intensity, (a), illustrating the speckle variance in a long exposure image. Panel (b) represents the theoretical limit of perfect PSF subtraction in a single exposure subject to MR intensity fluctuations. The photon-counting SSD algorithm results in the maximum likelihood estimates shown in (d), (g), and (j). Using a priori knowledge of the I_c parameter (we used a Gaussian prior of $\text{True } I_c \pm 3 \cdot \sqrt{\text{True } I_c}$) we generate the maximum a posteriori (MAP) estimates shown in (e), (h), and (k). The planet signals extracted from the MAP I_p estimate in (e) are not significantly improved compared to the MLE I_p in (d). However, the SSD results in (d) and (e) both extract the planet better than the perfect PSF subtraction shown in (b). All images represent 30 seconds of data on a magnitude $J = 10$ star with an 8.2 m telescope; all units are photons/second.

TABLE 1
COMPANION SSD SIGNAL-TO-NOISE RATIO

Contrast	Separation = $3.5 \lambda/D$			Separation = $6.5 \lambda/D$			Separation = $9.5 \lambda/D$			Separation = $12.5 \lambda/D$		
	MLE	MAP	Limit [†]	MLE	MAP	Limit [†]	MLE	MAP	Limit [†]	MLE	MAP	Limit [†]
$4 \cdot 10^{-4}$	4.8	5.3	2.3	6.8	7.0	3.8	7.6	8.3	5.7	7.0	9.4	8.8
$2 \cdot 10^{-4}$	2.8	3.0	1.2	4.0	4.0	1.9	4.9	4.9	2.9	5.6	5.9	4.5
$1 \cdot 10^{-4}$	1.6	1.7	0.6	2.3	2.3	1.0	2.8	2.8	1.4	3.5	3.5	2.3
$5 \cdot 10^{-5}$	0.9	0.9	0.3	1.3	1.2	0.5	1.6	1.5	0.7	2.0	2.0	1.1

[†] Detection limit for a 30 s long exposure with perfect PSF subtraction of the stellar light.

directly reduce I_c in the image.

On a space-borne telescope atmospheric speckles are not a concern, implying that the image-plane intensity will have different temporal behavior from ground-based observatories. While our SSD algorithm relies on the intensity following a MR distribution, in general any distribution can be used so long as it is known. It may also be possible to modulate speckles in a controlled way using onboard AO.

6. CONCLUSIONS

In this paper we exploit photon arrival time statistics with a stochastic speckle discrimination (SSD) algorithm to distinguish planets from speckles. We first extend previous work with a formalized maximum likelihood algorithm operating on light curves with fixed, albeit fast, exposure times. We find that the likelihood space can sometimes result in bimodal behavior in the case of $I_c \gg I_s$. Additionally, the choice in exposure time can systematically skew the MLE of I_p and inflate its variance. More generally, with a fixed exposure time, the performance will change as a function of parameters I_c , and I_s . This is a problem because I_c and I_s can change with observing conditions as well as with separation from the host star.

To overcome these difficulties, we have developed a new photon-counting SSD algorithm that calculates the maximum likelihood for I_p directly from the individual photon arrival times. With this approach the likelihood space becomes smooth and unimodal and the precision is maximized. The planet detection performance can be better by a factor of 2 than perfect stellar PSF subtraction of a long exposure. This requires fast noiseless detectors like MKIDs.

We have made several simplifying assumptions in our analysis. We take the speckle temporal PSD to be described by the single exponential timescale τ_s , we as-

sume I_c , I_s , and I_p to remain constant, and we assume that the MR distribution accurately describes the off-axis stellar intensity. Finally, we ignore chromaticity. These assumptions represent avenues of exploration for future work. The speckle temporal PSD can be measured and used to more accurately simulate photon lists. Since the instantaneous Strehl can be measured, a future implementation of this algorithm might include that as a priori information in the log likelihood model. This would also inform additional variance on I_p apart from the Poisson noise.

SSD algorithms are ultimately constrained on two fronts. First, the photon arrival time δt must be much shorter than the speckle decorrelation time τ_s : we need many photons to characterize the properties of a materialized speckle. Second, the performance degrades when I_c is large but I_s is small, because the incoherent planet light masquerades as the static speckles described by I_c . Fortunately, this can be improved with a coronagraph.

In return, SSD algorithms are most useful when I_s is large, which is often inescapable at small inner working angles. Furthermore, the results are not directly dependent on separation (although they are dependent on I_c and I_s , which are larger at small separations). This makes SSD a powerful post-processing technique at small inner working angles where it can complement more established techniques like ADI and SDI. At high speckle intensities, SSD can even outperform the theoretical limits of a perfect implementation of ADI and SDI.

This work was supported by the National Science Foundation Grant 1710385 and NASA ROSES grant NNX15AG23G. We would like to thank Michael Fitzgerald (University of California, Los Angeles) for helpful comments during the early stages of this work.

REFERENCES

- Aime, C., & Soummer, R. 2004, in 2004 12th European Signal Processing Conference, 1071
- Cagigal, M. P., & Canales, V. F. 1999, in Society of Photo-Optical Instrumentation Engineers (SPIE) Conference Series, Vol. 3866, Optics in Atmospheric Propagation and Adaptive Systems III, ed. A. Kohnle & J. D. Gonglewski, 165
- Cagigal, M. P., & Canales, V. F. 2001, Optical Engineering, 40, 2690
- Canales, V. F., & Cagigal, M. P. 1999, Appl. Opt., 38, 766
- DeLong, E., DeLong, D., & Clarke-Pearson, D. 1988, Biometrics, 44, 837–845
- Fitzgerald, M. P., & Graham, J. R. 2006, ApJ, 637, 541
- Frazin, R. A. 2016, Empirical green’s function approach for utilizing millisecond focal and pupil plane telemetry in exoplanet imaging
- Gerard, B. L., Marois, C., Currie, T., et al. 2019, arXiv e-prints, arXiv:1905.05821
- Gladysz, S., & Christou, J. C. 2008, The Astrophysical Journal, 684, 1486
- Gladysz, S., Yaitskova, N., & Christou, J. C. 2010, Journal of the Optical Society of America A, 27, A64
- Goebel, S. B., Guyon, O., Hall, D. N. B., et al. 2018, Publications of the Astronomical Society of the Pacific, 130, 104502
- Goodman, J. W. 1975, Statistical Properties of Laser Speckle Patterns, ed. J. C. Dainty (Berlin, Heidelberg: Springer Berlin Heidelberg), 9
- Guyon, O. 2005, The Astrophysical Journal, 629, 592
- Jensen-Clem, R., Mawet, D., Gonzalez, C. A. G., et al. 2017, The Astronomical Journal, 155, 19
- Kepler, M., Benisty, M., Müller, A., et al. 2018, A&A, 617, A44
- Krzanowski, W. J., & Hand, D. J. 2009, ROC Curves for Continuous Data (1st ed.) (Chapman & Hall/CRC)
- Kuzuhara, M., Tamura, M., Kudo, T., et al. 2013, ApJ, 774, 11
- Lafrenière, D., Marois, C., Doyon, R., Nadeau, D., & Artigau, É. 2007, ApJ, 660, 770

- Lagrange, A. M., Bonnefoy, M., Chauvin, G., et al. 2010, *Science*, 329, 57
- Lozi, J., Guyon, O., Jovanovic, N., et al. 2018, Scexao, an instrument with a dual purpose: perform cutting-edge science and develop new technologies
- Macintosh, B., Graham, J. R., Barman, T., et al. 2015, *Science*, 350, 64
- Macintosh, B., Poyneer, L., Sivaramakrishnan, A., & Marois, C. 2005, Speckle lifetimes in high-contrast adaptive optics
- Marois, C., Correia, C., Galicher, R., et al. 2014, in *Society of Photo-Optical Instrumentation Engineers (SPIE) Conference Series*, Vol. 9148, Adaptive Optics Systems IV, 91480U
- Marois, C., Doyon, R., Racine, R., & Nadeau, D. 2000, *PASP*, 112, 91
- Marois, C., Lafrenière, D., Doyon, R., Macintosh, B., & Nadeau, D. 2006, *ApJ*, 641, 556
- Marois, C., Macintosh, B., Barman, T., et al. 2008, *Science*, 322, 1348
- Martinache, F., Guyon, O., Jovanovic, N., et al. 2014, *Publications of the Astronomical Society of the Pacific*, 126, 565
- Mawet, D., Milli, J., Wahhaj, Z., et al. 2014, *The Astrophysical Journal*, 792, 97
- Mawet, D., Pueyo, L., Lawson, P., et al. 2012, Review of small-angle coronagraphic techniques in the wake of ground-based second-generation adaptive optics systems
- Meeker, S. R., Mazin, B. A., Walter, A. B., et al. 2018, *Publications of the Astronomical Society of the Pacific*, 130, 1803.10420
- Racine, R., Walker, G. A. H., Nadeau, D., Doyon, R., & Marois, C. 1999, *PASP*, 111, 587
- Soummer, R., Ferrari, A., Aime, C., & Jolissaint, L. 2007, *The Astrophysical Journal*, 669, 642
- Soummer, R., Pueyo, L., & Larkin, J. 2012, *ApJ*, 755, L28
- Sparks, W. B., & Ford, H. C. 2002, *ApJ*, 578, 543
- Stangalini, M., Causi, G. L., Pedichini, F., et al. 2018, Recurrence quantification analysis as a post-processing technique in adaptive optics high contrast imaging
- Stangalini, M., Pedichini, F., Ambrosino, F., Centrone, M., & Moro, D. D. 2016, Speckle statistics in adaptive optics images at visible wavelengths
- Tanner Jr., W. P., & Swets, J. A. 1954, *American Psychological Association*, 61, 401
- van Eyken, J. C., Strader, M. J., Walter, A. B., et al. 2015, *The Astrophysical Journal Supplement Series*, 219, 14
- Walter, A. B., Mazin, B. A., Bockstiegel, C., et al. 2018, Mec: the mkid exoplanet camera for high contrast astronomy at subaru (conference presentation)

APPENDIX

We derive here the noise of a long ($t_{\text{exp}} \gg \tau_s$) exposure subject to speckle statistics. This is not simply photon shot noise, but arises due to the fluctuations of the modified Rician itself. We consider a modified Rician parametrized by I_c and I_s with an exponential decorrelation time τ_s . The basic statistics of the distribution are

$$\langle I \rangle = I_c + I_s \quad (\text{A1})$$

$$\sigma_I^2 = \langle I^2 \rangle - \langle I \rangle^2 = I_s^2 + 2I_c I_s \quad (\text{A2})$$

$$\langle (I_i - \langle I \rangle)(I_j - \langle I \rangle) \rangle = \sigma_I^2 \exp \left[-\frac{|t_i - t_j|}{\tau_s} \right]. \quad (\text{A3})$$

We wish to compute the variance of the mean intensity measured over a finite time interval T_{tot} , which we divide into N subintervals, each of length δt .

$$\bar{I} = \frac{1}{N} \sum_i I_i. \quad (\text{A4})$$

This is

$$\langle \bar{I}^2 \rangle - \langle \bar{I} \rangle^2 = \frac{1}{N^2} \left\langle \sum_i \sum_j I_i I_j \right\rangle - \frac{1}{N^2} \left\langle \sum_i I_i \right\rangle^2 \quad (\text{A5})$$

$$= \frac{1}{N^2} \left\langle \sum_i \sum_j (I_i - \langle I \rangle) (I_j - \langle I \rangle) \right\rangle \quad (\text{A6})$$

$$= \frac{\sigma_I^2}{N^2} \sum_i \sum_j \exp \left[-\frac{|t_i - t_j|}{\tau_s} \right]. \quad (\text{A7})$$

Now we will set $t_i = i\delta t$. For the third step below, we use $\delta t/\tau_s \ll 1$. More generally, we take $\delta t \rightarrow 0$, $N \rightarrow \infty$.

$$\frac{1}{N^2} \sum_i \sum_j \exp \left[-\frac{|t_i - t_j|}{\tau_s} \right] = \frac{1}{N^2} \sum_i \sum_j \exp \left[-\frac{|i - j|\delta t}{\tau_s} \right] \quad (\text{A8})$$

$$= \frac{1}{N^2} \sum_{i=0}^{N-1} \left(\sum_{j=0}^{N-i-1} \exp \left[-\frac{j\delta t}{\tau_s} \right] + \sum_{j=0}^i \exp \left[-\frac{j\delta t}{\tau_s} \right] - 1 \right) \quad (\text{A9})$$

$$= \frac{1}{N^2} \sum_{i=0}^{N-1} \left(\frac{\tau_s}{\delta t} \left(2 - \exp \left[-\frac{(N-i)\delta t}{\tau_s} \right] - \exp \left[-\frac{(i+1)\delta t}{\tau_s} \right] \right) - 1 \right) \quad (\text{A10})$$

$$= \frac{2\tau_s}{N\delta t} - \frac{2\tau_s}{N\delta t} \frac{1}{N} \left(\sum_{i=1}^N \exp \left[-\frac{i\delta t}{\tau_s} \right] \right) - \frac{1}{N} \quad (\text{A11})$$

$$= \frac{2\tau_s}{N\delta t} - 2 \left(\frac{\tau_s}{N\delta t} \right)^2 \left(1 - \exp \left[-\frac{(N+1)\delta t}{\tau_s} \right] \right) + \frac{2\tau_s}{N^2\delta t} - \frac{1}{N}. \quad (\text{A12})$$

Taking $N \rightarrow \infty$, $\delta t \rightarrow 0$, and $N\delta t = T_{\text{tot}}$, we have

$$\langle \bar{I}^2 \rangle - \langle \bar{I} \rangle^2 = \left(\frac{2\tau_s}{T_{\text{tot}}} - 2 \left(\frac{\tau_s}{T_{\text{tot}}} \right)^2 \left(1 - \exp \left[-\frac{T_{\text{tot}}}{\tau_s} \right] \right) \right) \sigma_I^2 \quad (\text{A13})$$

$$= \left(\frac{2\tau_s}{T_{\text{tot}}} - 2 \left(\frac{\tau_s}{T_{\text{tot}}} \right)^2 \left(1 - \exp \left[-\frac{T_{\text{tot}}}{\tau_s} \right] \right) \right) (I_s^2 + 2I_c I_s). \quad (\text{A14})$$

In the limit of a very short integration, $T_{\text{tot}} \ll \tau_s$, the prefactor is unity (as expected). For an integration time much longer than the decorrelation time, $T_{\text{tot}} \gg \tau_s$ (as is more typical), Equation (A14) simplifies to

$$\langle \bar{I}^2 \rangle - \langle \bar{I} \rangle^2 \approx \left(\frac{2\tau_s}{T_{\text{tot}}} \right) (I_s^2 + 2I_c I_s). \quad (\text{A15})$$

Assuming $2I_s\tau_s \gg 1$ (the inter-photon arrival time from the speckle field is much shorter than the decorrelation time τ_s), Equation (A14) dominates over simple shot noise $\sigma^2 = (I_c + I_s)/T_{\text{tot}}$. Interestingly, setting the number of independent realizations of the modified Rician equal to T_{tot}/τ_s would miss the factor of two in Equation (A15). Adding shot noise back in, assuming $T_{\text{tot}} \gg \tau_s$, and including a component I_p incoherent with I_c and I_s , we have

$$\sigma_{I,\text{tot}}^2 \approx \frac{2\tau_s (I_s^2 + 2I_c I_s) + I_c + I_s + I_p}{T_{\text{tot}}}. \quad (\text{A16})$$